Density Reconstruction in Convergent High-Energy-Density Systems Using X-Ray Radiography and Bayesian Inference

S. Ressel,[1, a)] J. J. Ruby,[1, 2, b)] G. W. Collins,[1, 2, 3] and J. R. Rygg[1, 2, 3]
[1)]*Laboratory for Laser Energetics, University of Rochester, Rochester, New York, 14627, USA*
[2)]*Department of Physics and Astronomy, University of Rochester, Rochester, New York, 14627, USA*
[3)]*Department of Mechanical Engineering, University of Rochester, Rochester, New York, 14627, USA*

(Dated: 2 February 2022)

X-ray radiography is a technique frequently used to diagnose convergent high-energy-density (HED) systems such as inertial confinement fusion implosion; and provides unique information that is not available through self-emission measurements. We investigate the scope and limits of that information using a radiography simulation combined with Bayesian inference workflow. The accuracy of density reconstruction from simulated radiographs of spherical implosions driven with 20 kJ laser energy is assessed, including the increase or decrease in accuracy due to the addition of Lagrangian marker layers, Poisson noise, and improved prior information. This work is the first to present the full uncertainty distributions inferred from radiography analysis in HED systems and demonstrates the importance of constructing the full posterior probability density, as opposed to a point estimate, due to the modal structure of the likelihood surface introduced by typical experimental noise sources. This general methodology can be used both for robust analysis of radiographic data and for improved design of radiography experiments by modeling the full experimental system.

I. INTRODUCTION

X-ray radiography is an imaging technique that uses high-energy photons (tens to hundreds of keV) to probe the interior of an object. This technique first emerged in the late 19th century with the discovery of x-rays by Wilhelm Röntgen[1], and almost immediately following his discovery Röntgen and other scientists realized the potential applications of X-rays to medicine and to a variety of other research areas. The medical field in particular has driven substantial development in reconstruction techniques such as inversion[2] and forward modeling.[3] X-ray radiography in combination with similar reconstruction techniques is also commonly used within engineering to nondestructively investigate material properties and structures[4] and items such as rock samples.[5]

Radiography has also long been applied to high-energy-density (HED) systems. Early work used time-resolved x-ray radiography to study radiation-driven shock propagation and interface mixing in planar targets, which has applications in inertial confinement fusion (ICF).[6] ICF research has also been one of the primary drivers for improving radiography technology and reconstruction methods since there are a number of important metrics that can be measured from radiography experiments. A common integral transform inversion technique known as Abel inversion has been used to infer fuel layer density distributions,[7] which govern several of the aforementioned metrics including shock velocity and target mass. Forward-fitting techniques such as those employed in Bayesian inference have also been applied to ICF systems to overcome information deficits associated with Abel inversion in spherical implosion geometry and have extracted information about important integrated ablator quantities like areal density $\langle \rho R \rangle$, average radius $\langle R \rangle$, and mass $\langle M \rangle$ of a spherical shell target.[8] Additional work has employed modified radiography techniques such as refraction-enhanced radiography and phase-contrast imaging[9] to infer density gradients in in-flight capsules[10] and for studying discontinuities at interfaces and shock fronts.[11]

More recently, radiography has been applied to absolute equation-of-state (EOS) measurements.[12–14] Forward-fitting methods have been employed to determine the shock velocity and compression of spherical targets, which can then be related to pressure through the Rankine-Hugoniot equations.[15] This allows for an absolute measurement of the mechanical state on the shock Hugoniot,[12] and these high-energy-density states are relevant to studying many astrophysical contexts including stellar evolution and the interior structure of white dwarf stars.[14] A critical aspect of this work is the ability to uniquely identify the density distribution (profile) at the location of the shock wave from a radiograph.

This work expands on previous efforts to extract information about density profiles in convergent HED systems using x-ray radiography by using a straight-line ray-trace coupled with a forward-fitting Bayesian inference algorithm. This combination of computational tools provides an avenue to investigate the importance of different aspects of the experimental design when attempting to reconstruct target density profiles and to understand the full uncertainty associated with the reconstruction. As an example, this work investigates a single strong shock wave launched in a solid hydrocarbon sphere at the scale relevant to the OMEGA[16] Laser located at the University of Rochester's Laboratory for Laser Energetics. A

[a)]Currently at Department of Atmospheric Sciences, University of Washington
[b)]Currently at Lawrence Livermore National Laboratory; Electronic mail: ruby4@llnl.gov

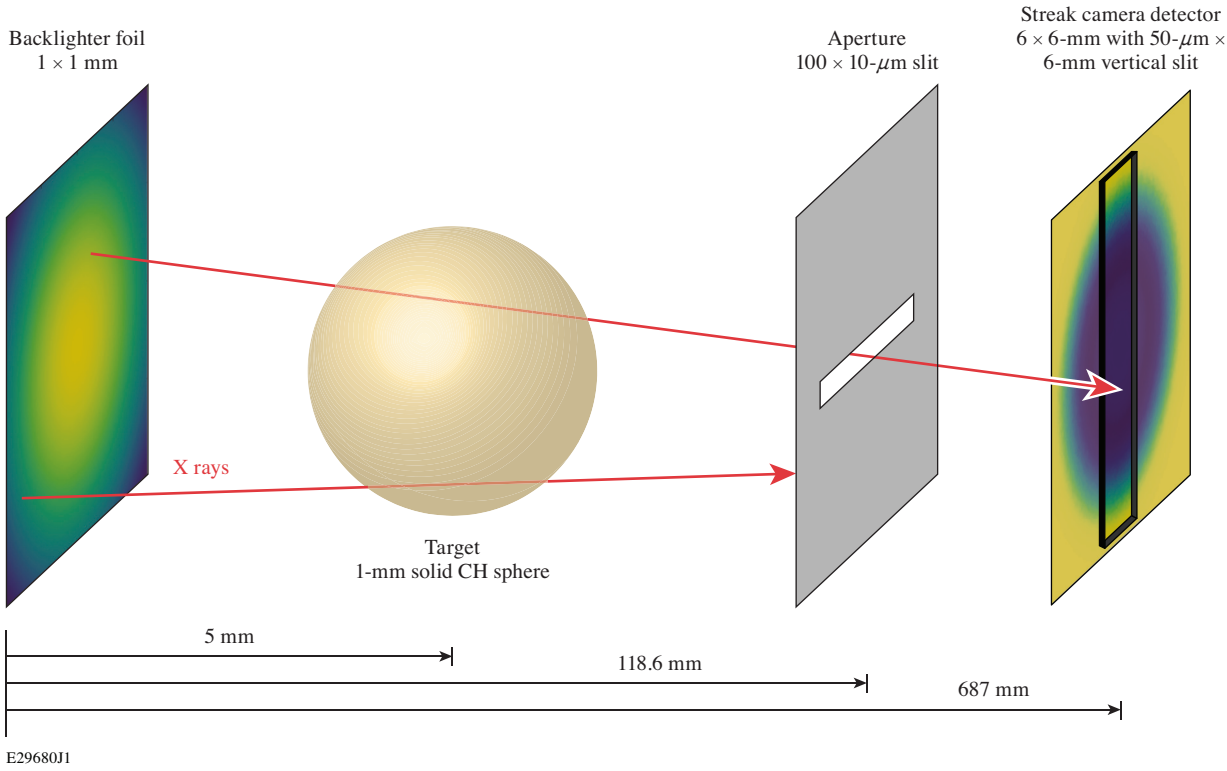

FIG. 1. A schematic showing the setup of a standard streaked radiography experiment on the OMEGA Laser, with typical distances and sizes given (not to scale). A backlighter with some intensity profile emits rays, which transit an object to be imaged. The rays are attenuated by the object, which (in this work) has no self-emission, and then pass through an imaging slit to achieve spatial resolution. The rays then land on a detector where a sub-region is selected by another slit in the complementary orientation to the imaging slit to represent the streak camera collection slit (which provides temporal resolution) and are binned on a detector. The target is initially uniform density but will have some radial density profile once a shock wave is generated using the spherical laser drive of Omega.

simulation by the 1-D radiation-hydrodynamic code *LILAC* is used to generate thermodynamic profiles in time and space to test the precision and accuracy of the density reconstruction.

Sections II and III detail the ray-trace that was used and give a brief primer on the Bayesian inference algorithm implemented. Section IV describes a simple test case for the ray-trace and density reconstruction, and Sec. V details the reconstruction of the density profile generated by the *LILAC* code. Finally, Sec. VII discusses the relevance of these results and possible future work that would further extend the results presented here.

II. SIMULATION DETAILS

This analysis scheme includes a straight-line ray-trace coupled to a full Bayesian inference infrastructure, expanding the use of Bayesian methods employed in previous works[8,12,17,18] to include a full forward simulation of the system and a sampling of the full posterior distributions. The previous works borrowed techniques from Bayesian inference, such as regularization,[8] to constrain their models using point estimates such as maximum likelihood estimation (MLE) with uncertainty estimates following from local perturbations around the MLE estimate of the model parameters,[12] or by evaluating a number of repeat experiments.[8] This work expands on these techniques by producing the full posterior probability distributions of the model parameters for a single measurement.

The ray-trace component of the workflow begins by generating rays at a reference plane, in this instance the backlighter used for the radiography, with a given location, direction, and initial intensity based on the spatial distribution of the backlighter. The rays are propagated in space at a fixed time through the converging target where the equation of radiative transfer is solved along each ray using a node-centered discretization. The target is defined by 3-D density, temperature, and mass absorption coefficient distributions; this process models the absorption and emission of rays by the object the rays intersect. The change in the monochromatic spectral radiance, I_ν (W sr^{-1} m^{-2} Hz^{-1}) of each ray as it propagates through the target is described by the (differential) equation of radiative transfer[19]

$$\vec{\Omega}\cdot\vec{\nabla}I_\nu = \rho\,\kappa_\nu^{'}\,(S_\nu - I_\nu)\,, \tag{1}$$

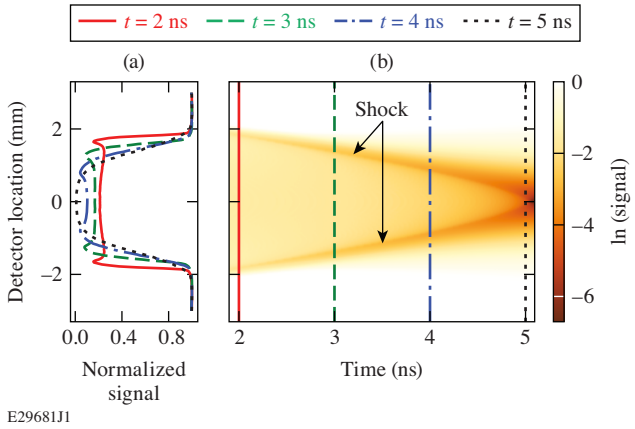

FIG. 2. (a) A series of spatially-integrated, time-resolved radiographic lineouts that correspond to the lines in (b) which shows a simulated x-ray streak image of an OMEGA-scale implosion generated using the straight-line ray-trace simulation and reference data taken from the 1-D radiation-hydrodynamic code *LILAC*. At each time the process from Fig. 1 generates a single vertical lineout in (b) which are collected together to produce the full streak history. The trajectory of the shock in time can be clearly seen, given by the 2 dark limbs converging to the central axis.

$$\kappa_\nu^{'} = \kappa_\nu \left(1 - e^{-\frac{h\nu}{k_B T}}\right), \tag{2}$$

where $\vec{\Omega}$ is the angular distribution of the ray, ρ is the density in g cm^{-3}, κ is the opacity in cm^2 g^{-1}, T is the temperature in K, ν is the frequency of light being considered in Hz, and S_ν is the source function, which can be neglected for the case of no self-emission used in this work. This casting of the equation omits the temporal dependence of the spectral radiance since the time scales of ray propagation [$\approx 0.001(\text{m})/c$] are smaller than the dynamical times scales of the target being considered ($\approx$ tens to hundreds of ps). After the equation of radiative transfer is solved, the rays are apertured and binned into detection elements, simulating a typical measurement apparatus such as an x-ray streak camera[20] or x-ray framing camera.[21] Figure 1 demonstrates this process; how rays start from the backlighter plane (far left), propagate through the 3-D target region (center left), pass through or are blocked by the aperture slit (center right), and eventually are binned in the detector plane (far right) to form a 2-D image.

Fully modeling the detection system is one of the strengths of using a ray-trace since it avoids convolving the measured signal with an assumed response and allows for the multidimensional effects of the aperture (such as rotations and integrating over non-imaging dimensions) to fold naturally into the analysis. This process results in a radiant flux that is spectrally integrated and multiplied by the pixel area to produce radiant energy per detector pixel. By default, the simulation neglects noise, but the Poisson noise associated with photon-counting experiments is explicitly added in Sec. VI C.

Although the ray-trace is performed at a single instance in time, a time-resolved streak image can be generated by repeating this process at different times. A number of single-time radiographic lineouts can be seen in Fig. 2(a), and the full time-resolved 2-D radiograph can be seen in Fig. 2(b). In all examples considered in this work, including those in Fig. 2, radiographs and radiographic lineouts (henceforth called "lineouts") are normalized so that maximum signal corresponds to a value of 1. This is also true for the reference lineouts generated by the ray-trace using the *LILAC* thermodynamic profiles.

III. BAYESIAN INFERENCE

The Bayesian inference scheme implemented in this work draws inspiration from previous work in HED science.[22–24] Since many in-depth explanations of Bayesian inference are available, one will not be presented here, although a brief explanation is warranted. For the purposes of the work considered, the following Bayesian inference procedure was employed:

1. Given a reference lineout (experimental or synthetic), determine a parameterization of the density profile to be reconstructed and any other relevant parameters (such as opacity). Specify *a priori* distributions for each parameter of the parameterization.

2. Use the ray-trace simulation to generate a synthetic lineout corresponding to the parameterization chosen, drawing a set of parameter values randomly from the prior distributions.

3. Statistically compare the synthetic lineout to the reference lineout using a likelihood function. The choice of likelihood function depends on the data, so here a Gaussian likelihood with some width σ is appropriate.

4. Based on the statistical comparison of the two lineouts, generate a posterior probability value for each parameter.

This process is repeated with a specified number of initial parameter guesses or *draws* and the result is an N-dimensional posterior probability distribution in parameter space, where N is the number of parameters. The final posterior distribution is generally interpreted as the result of a continuous updating of the prior values given the evidence of the likelihood calculation. A number of statistical methods can then be applied to analyze the data and interpret the posterior distribution. Specifically, a marginalized probability distribution can be determined for each parameter θ_i through the following equation:

$$P(\theta_i) = \int_{\theta_{j\neq i}} P(\theta_i \,|\, \theta_1, \theta_2, ..., \theta_N) \times P(\theta_1, \theta_2, ..., \theta_N)\, d\theta_j \tag{3}$$

Essentially, $P(\theta_i)$, the marginalized probability distribution of parameter θ_i, is the integral of the full probability distribution integrated over all parameters that are not θ_i.

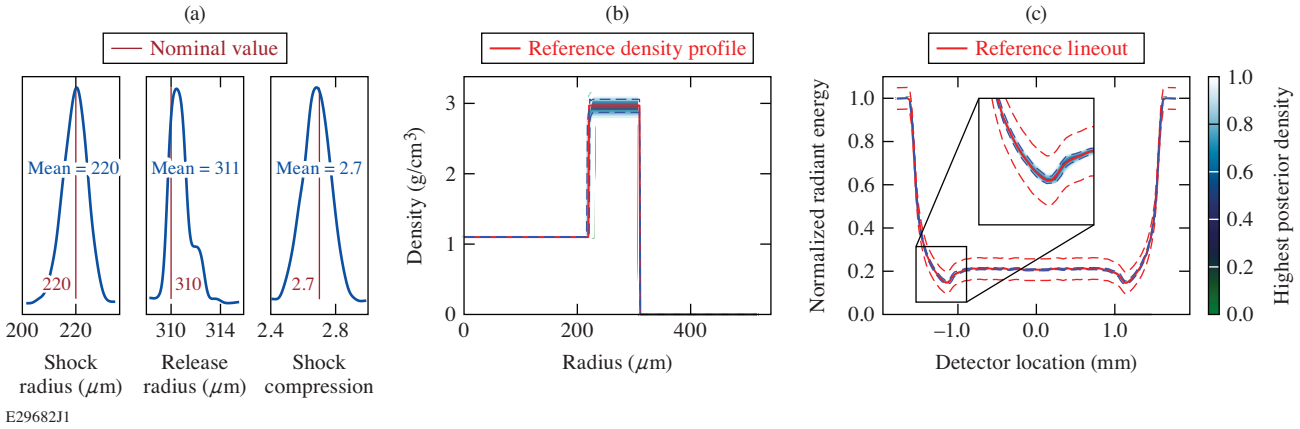

FIG. 3. (a) Posterior distributions for each of the three parameters of the simple model given in Eq. (6), as well as (b) the posterior predictive distributions (PPD's) of the density profile, constructed by sampling the posteriors from (a), and (c) lineouts generated from the density PPD's distributions. The color scales in (b) and (c) show highest posterior density intervals (HPD), the shortest region that contains a given amount of probability. The posterior distributions in (a) are well matched to their reference data, given by the vertical dark-red lines. Additionally, PPD's of the lineouts have been constrained by the inference process and are well matched to the reference lineout, especially around the minimum highlighted in the inset of (c). The dashed lines in (c) give the scale of σ used in the Likelihood function (e.q. 4). The PPD's of the density profile are also well matched to the reference density. Although the reference density is known explicitly in this example, it is not used as part of the inference nor generally known *a priori*.

A. Likelihood Function

The likelihood function is a measure of the probability of observing the given data presupposing a correct model. Therefore, the choice of likelihood function is highly dependent on the type of the data and the model. For this experimental setup, the reference lineout is the result of a Poisson process, and the uncertainty associated with the reference data should therefore follow a Poisson distribution. In the limit of large photon counts, however, as is the case in the simulation, the Poisson distribution converges to a Gaussian distribution, so a Gaussian likelihood function is an appropriate way to represent the relationship between the data and the model. The width of the Gaussian, σ, is a measure of the uncertainty of the reference data. The likelihood function, L, is given in Eq. (4):

$$L = \exp\left[-\frac{1}{2}\sum\frac{(\text{data}-\text{model})^2}{\sigma^2}\right]. \tag{4}$$

In practice, the natural logarithm of Eq. (4) is usually taken, so that the Bayesian inference occurs on

$$\ln(L) = -\frac{1}{2}\left[\sum\frac{(\text{data}-\text{model})^2}{\sigma^2}\right], \tag{5}$$

where the data are the reference lineout, the model is the synthetic lineout generated by the ray-trace for a given set of sampled parameters, and the summation occurs over all detector locations at a given instance in time. For *LILAC*-generated reference data without noise, a constant value of 0.05 was used for σ. In cases where Poisson noise was applied explicitly to the reference, the uncertainty σ was calculated as a function of the normalized signal. This has the effect that areas of lower signal have more uncertainty, which is a realistic result of a Poisson process on experimental data.

IV. SIMPLE MODEL EXAMPLE

A simplified model consisting of a steady spherically converging shock wave using a two-step radial density profile is used to demonstrate the analysis workflow and results. The density model used is

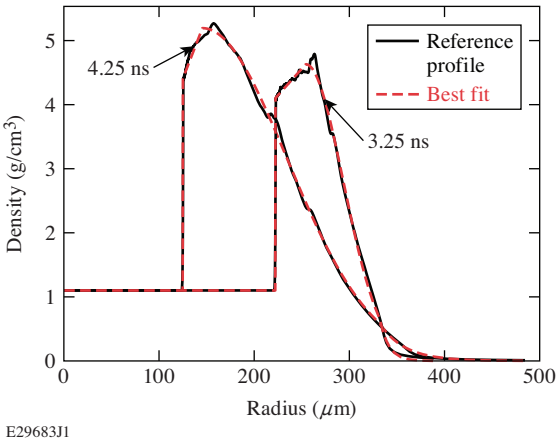

FIG. 4. *LILAC* radiation-hydrodynamic simulation density profiles (black curve) of a 1-mm-diameter solid CH ball driven with 27 kJ at times $t = 3.25$ ns and $t = 4.25$ ns. The profiles are well represented by the best-fit model using Eq. (7) (red curve).

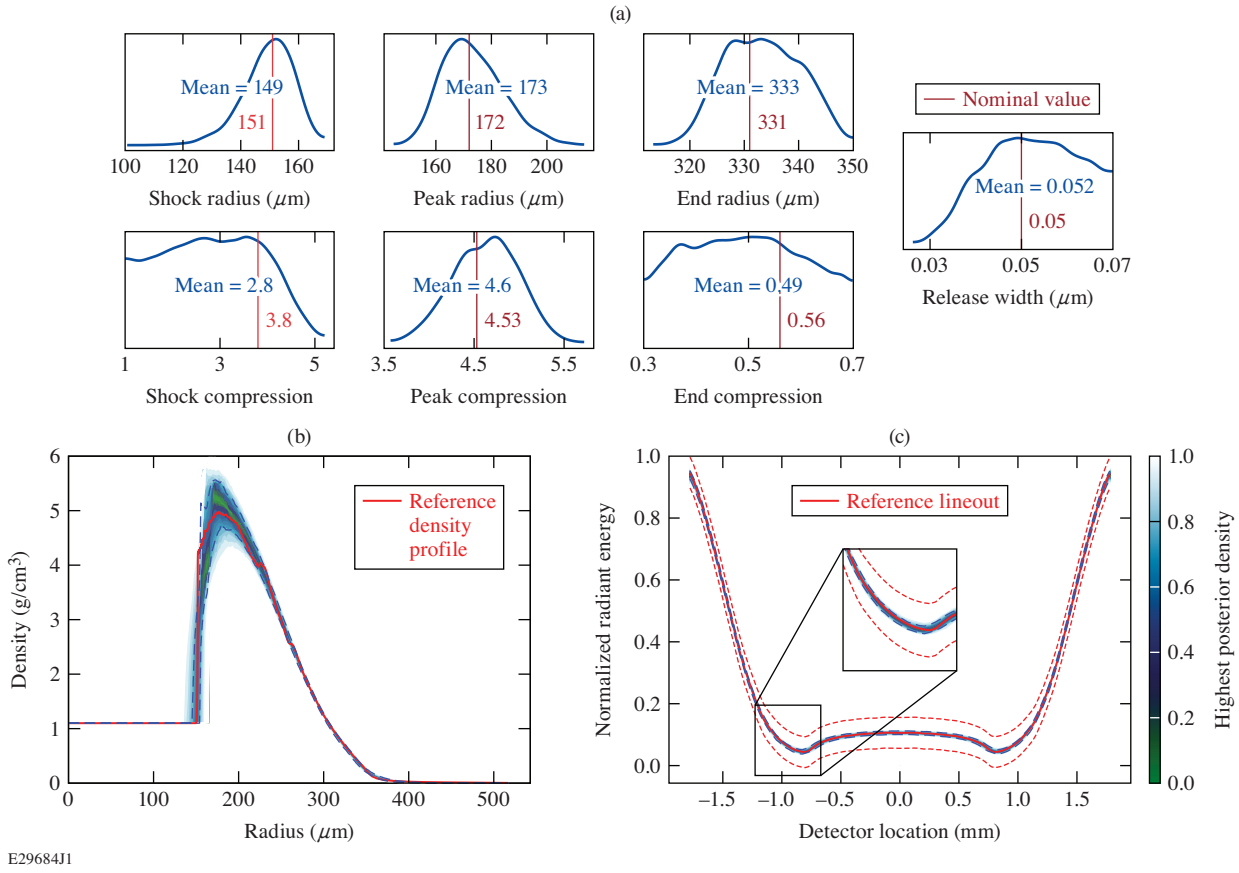

FIG. 5. (a) Posterior distributions for each of the seven parameters of the model given in Eq. (7), as well as (b) PPD's of the density profiles and (c) lineouts generated from said posterior distributions. A number of the parameters are well constrained, as shown by a single narrow peak in their posterior distributions, including the location of the shock, the location of the peak density, and the peak compression and they all recover the underlying nominal value, given by the vertical red line, which is the least-squares best fit value recovered by fitting the simulated density profile with the assumed model (like in Fig. 4). Notably, the posterior distribution for the shock compression (ρ_s/ρ_0) is not well-constrained, presenting an upper bound of about 4, but roughly equal probability density across all values below 4. This can also be seen in (b), which is well matched to the reference density profile outside the region of the shock. Despite this, the PPD's of the lineouts in (c) are converged from the inference and well matched to the reference information even around the feature due to the shock limb highlighted in the inset. The dashed lines in (c) give the scale of σ used in the Likelihood function (e.q. 4).

$$\rho(r) = \begin{cases} \rho_0 & \text{for } r < r_{\text{shock}} \\ \eta\rho_0 & \text{for } r_{\text{shock}} < r < r_{\text{release}} \\ 0 & \text{for } r > r_{\text{release}} \end{cases}, \tag{6}$$

where ρ_0 is treated as a fixed known value of initial density, r_{shock} is the radial position of the shock, η is the compressibility given by the ratio of the density before and after the shock passes, and r_{release} is the radial position at which there is no longer any material. This simple parameterization, which is easy to interpret and computationally efficient, serves as a useful test case of the analysis workflow in a setting where reference data can be generated with known parameters. Specifically, the values for this example are $\rho_0 = 1.1$ g cm^{-2}, $r_{\text{shock}} = 270$ μm, $r_{\text{release}} = 310$ μm, and $\eta = (\rho_s/\rho_0) = 2.7$. Additionally, the correct density model can be applied within the Bayesian inference to decouple parameterization-based errors from other problems within the workflow. In combination, this allows one to exactly evaluate the performance of the inference. In this case the density model has a flat radial profile within the shocked region rather than an increasing density as would result from convergence effects in more realistic scenarios explored in Sec. V, but this has no effect on the workflow itself.

The inference process results in the posterior probability density distributions (henceforth called posteriors) for each of the 3 model parameters, shown in Fig. 3(a), which can be used to construct Posterior Predictive Distributions (PPD's) for the radial density profile, shown in Fig. 3(b). The lineouts used in the inference procedure explained in Sec. III to constrain the posteriors, and which correspond to the PPD's of the density profile, can be seen in Fig. 3(c). From the figures, it can be determined that the posterior distributions for each of the three parameters are well-constrained. Additionally, the PPD's of

the density profiles and lineouts generated are well matched to their respective references. Thus, the Bayesian inference procedure is able to successfully constrain the reference density profile and recover the model parameters.

V. ANALYSIS OF *LILAC* DATA

The inference workflow is tested on more-realistic data generated from the 1-D radiation hydrodynamic code *LILAC*, where a single spherically converging shock wave was simulated in a solid hydrocarbon sphere (CH) driven by 27 kJ of UV light using the *SESAME* 7592 EOS table[25] and Los Alamos astrophysical opacity tables.[26] The resulting radial density profiles are used to generate a simulated radiograph, as shown above in Fig. 2(b), to determine how much information about the density profile is encoded in the lineout, and to what extent the density profile can be reconstructed from lineout data.

All of the reference lineouts generated from the *LILAC* profiles are taken at a single time, $t = 4.0$ ns in Fig. 2. Additionally, the simulation was configured to model an idealized and typical setup of an OMEGA60 experiment with $5\times$ magnification, a spatially uniform backlighter intensity, and a perfect 10×100 μm slit projecting an image onto a detector with 27 μm pixels. In all examples the projection is then integrated in the less-resolved dimension to produce a single lineout on which the inference is performed. The opacity of the target in the ray-trace is taken as a constant, which is known for the purposes of the analysis here, so there is no effect due to the opacity on the inferred density profile (equivalently the inferred profiles can be consider to be $\kappa\rho$, the opacity density product rather than simply ρ but for purposes of discussion the opacity is assumed to be known here and mass density is used).

This system has a number of simplifications over a true experimental system that make it a best-case scenario for the purposes of inference and extracting information from the radiograph. Notably, these simplifications include not having to infer a backlighter intensity profile, using a truly monochromatic radiographic signal, the use of a known opacity, having no threshold on the signal contrast in the detector, and having no spatial blurring due to finite detection times and movement of the shock wave. Fully resolving any of the previously mentioned assumptions would lead to reduced performance of the inference process.

A. Density Profile Parameterization

The parameterization used to represent the *LILAC* density profile is similar in form to previous work[12] and is given by

$$\rho(r) = \begin{cases} \rho_0 & \text{for } r < r_s \\ \rho_s + (\rho_p - \rho_s)\left(\frac{r-r_s}{r_p-r_s}\right) & \text{for } r_s < r < r_p \\ \rho_p \cdot \exp\left(-\frac{(r-r_p)^2}{2\sigma^2}\right) & \text{for } r_p < r < r_e \\ \rho_e \cdot \exp\left(-\alpha(r-r_e)\right) & \text{for } r_e < r. \end{cases} \tag{7}$$

$$\sigma = \sqrt{-\frac{(r_p - r_e)^2}{2\ln(\rho_e/\rho_p)}}, \tag{8}$$

where r_s, r_p, and r_e are the radial locations of the shock, peak density, and tail, respectively; ρ_0, ρ_s, ρ_p, and ρ_e are the densities of the material in ambient conditions, immediately after being shocked, at its maximum due to converging flows, and at the tail of the density profile, respectively; and α is a scale parameter that determines how quickly the density reduces to 0 in the tail. The parameterization is designed for the density to be continuous, except at the location of the shock, and to explicitly include physical quantities of interest. In particular, the location of the shock front, r_s, and the density value immediately behind the shock front, ρ_s, can be used in combination to determine the equation of state of the material given a streaked radiograph.[12] An optimized density profile parameterization (to match the *LILAC* profile) is shown in Fig. 4 along with the underlying *LILAC* profiles for two different times, which show good agreement. Outside of this window of times, the density profile parameterization is unable to fully match the underlying profile, particularly in the tail, but this work will focus on inference from particular time slices that fall within the well-behaved window.

B. Constraints on Bayesian Inference

A primary benefit of using Bayesian inference is the ability to leverage as much information in the workflow as possible. This can occur through multiple different channels including the choices of prior distributions as well as additional terms added to the likelihood function to account for different constraints. In the examples shown here, largely uninformed priors (in the form of uniform distributions) with bounds based on physical considerations are used. The one exception is that of the radial location of the shock, which is given a Gaussian prior distribution around the location visible in the reference radiograph, such as at a time of $t = 4.0$ ns, where the shock occurs at a distance of approximately 0.796 mm from the central vertical axis of the detector in Fig. 2(a). Additional constraints include physicality considerations on the radial locations of the shock, peak, and tail, such that the shock occurs before the peak location, which itself occurs before the tail location, as well as a constraint ensuring that the peak compression is higher than the shock compression. These constraints

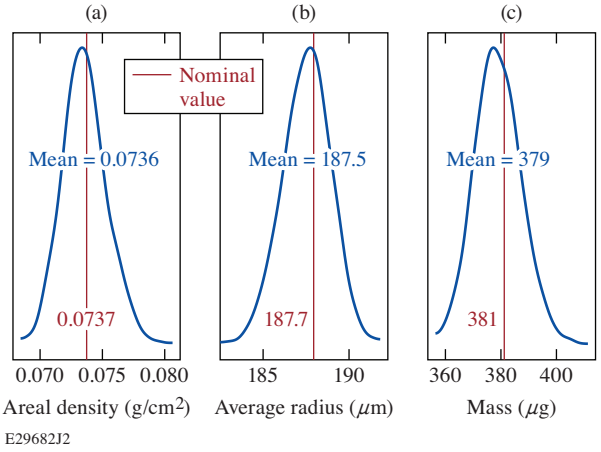

FIG. 6. PPD's of the first three moments of the density distribution. (a) The zeroth moment areal density in g cm^2, (b) the ratio of the first and zeroth moments, average radius in μm, and (c) the second moment, mass in μg. The mean values for each distribution are within 1% of their respective true value, which shows that they are well constrained despite the discrepancies in the density profile around the location of the shock. The widths of each moment's distribution is of order 5% when looking at the bulk of the distribution (i.e. the inflection point denoting the tails), which is much smaller than the 25% width seen in the peak compression posterior in Fig. 5.

serve to ensure that the resulting density profiles follow the physical intuition that led to the parameterization.

VI. EXAMPLE INFERENCE CASES

This section gives a series of inference examples that consider different experimentally relevant constraints. The first is the nominal case as described in Sec. V, the second includes the addition of a mass marker layer, the third includes simulated noise, and finally the fourth considers an outside constraint on the density immediately behind the shock.

A. Inference in Nominal Case

The first inference test includes the priors described in Sec. V B for the parameters of the density profile and the constraints on those parameters, but no additional constraints. The resulting posterior distributions for each of the seven parameters can be seen in Fig. 5(a), while the corresponding PPD's of the density profiles and lineouts can be seen in Figs. 5(b) and 5(c), respectively. The PPD of the lineout is well converged from the sampling around the reference lineout (red curve) used in the inference, showing that the model used was adequate to reproduce the full output; similarly, the entirety of the density profile is fairly well predicted with the exception of the region right around the shock jump.

Looking at the posteriors for the different model parameters in Fig. 5(a) shows that the specific value of the compression at the shock jump is not well constrained by the information in the lineout. An upper limit is placed on the distribution, but this is due to the explicit constraint that the shock compression must be less than the peak compression. The peak compression achieved is well constrained along with the location of the peak since much of the mass is in this bulk of the material, along with much of the areal density, the primary moment of the density distribution when considering absorption. These findings reinforce earlier work[8] describing radiographic reconstruction in imploding shells and the importance of the radial moments of the density distribution, the first three of which are given by[8] areal density $\langle \rho R \rangle$, average radius $\langle R \rangle$, and mass $\langle M \rangle$. The inferred distributions for these quantities are shown in Fig. 6 and, as suggested in this previous work,[8] these first three radial moments of the density distribution are well constrained by the radiographic measurement. Specifically, the mean values for each distributions recover the underlying true value to better than 1%, despite the large discrepancies in the density profile around the location of the shock seen in Fig. 5(a).

B. Lagrangian marker

The recent work on EOS measurements using radiography[12–14] employed a Lagrangian marker to introduce an added constraint on the system. The marker acts as a position tracer where the mass interior to the marker is known from initial conditions, providing an additional constraint from conservation of mass such that at all times the mass interior to this marker layer is known. This constraint comes in the form of an integral equation for the density profile,

$$M_{\text{marker}} = 4\pi \int_0^{r_{\text{marker}}} \rho(r) r^2 dr, \tag{9}$$

where M_{marker} and r_{marker} are the the total mass interior to the marker layer and the position of the marker layer, respectively.

This constraint was added to the Bayesian workflow used in the Sec. VI A by assuming the position of the marker layer is known and adding an additional term to the likelihood function that gives preference to profiles that satisfy the condition from Eq. (9), assuming a 5% normally distributed uncertainty on M_{marker}. The additional parameters required to describe the location of the marker layer are omitted here and the position of the marker layer is used as a known quantity with no uncertainty.

Figure 7(a) shows a comparison of the posteriors inferred from the case without a Lagrangian marker and the case with a Lagrangian marker at $r_{\text{marker}} = 260$ μm, for the shock compression, peak compression, and peak radius. There is little difference between the posteriors, except for a slight narrowing of the peak compression posterior, meaning that the information contained in the marker layer condition is largely degenerate with information that exists within the lineout. This is demonstrated in Fig. 7(b), which shows the PPD of the mass integrated up to the marker layer for the nominal situation without the explicit constraint (blue curve) and when the

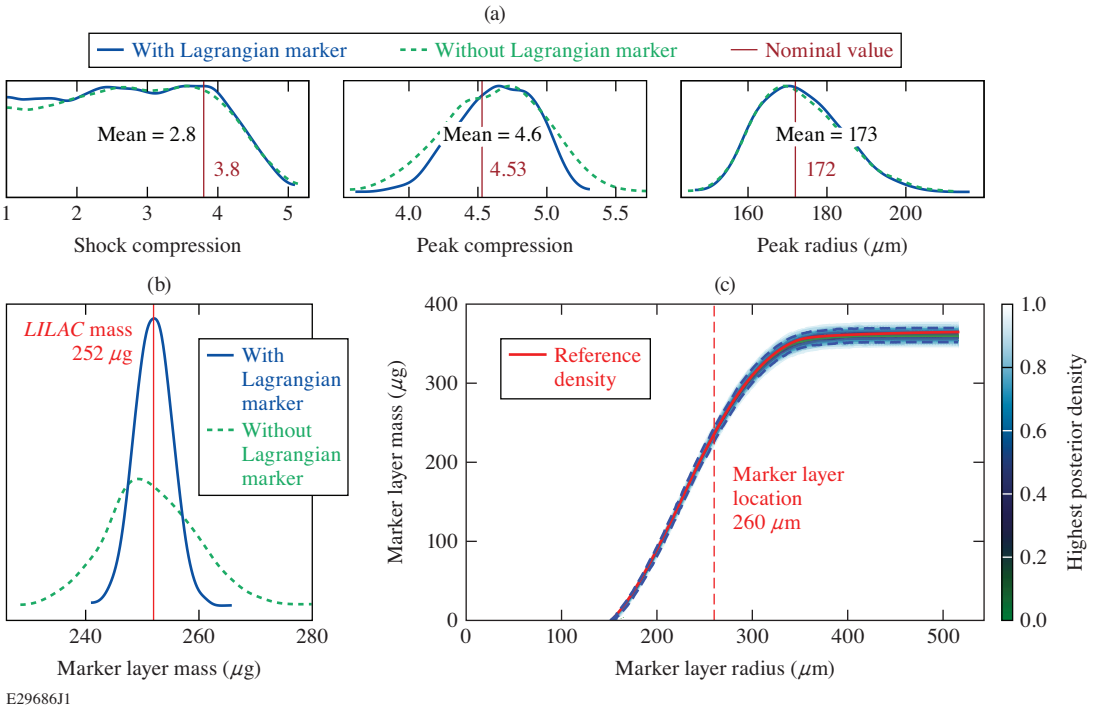

FIG. 7. (a) A comparison of the posterior distributions of select parameters inferred for the case with (solid blue) and without (dashed green) a Lagrangian marker. (b) Posterior Distributions of marker layer mass the case without a Lagrangian marker (blue) and with a Lagrangian marker (dashed green), as well as the value calculated using the reference *LILAC* density profile. This shows that even without the explicit constraint of a Lagrangian marker the integrated mass up the reference point is already strongly constrained, though the addition of the marker layer does narrow the distribution which coincides with the narrowing of the peak compression distribution in (a) meaning additional information gained from the marker layer contributes to better constraint of the peak density achieved behind the shock. (c) Marker layer mass (μg) (y-axis) as a function of a variable marker layer radius (μm) (x-axis) for the case with no Lagrangian Marker. Although the inference was performed without a marker layer constraint, the PPD's of the density profiles have integrated masses that are consistent with the true profile across various radii, showing that the Lagrangian marker does not contribute much additional information regardless of proximity to the shock front. Also shown in red dashes is the location of the marker layer used in the case with a Lagrangian Marker.

marker layer constraint is used (green curve). In both cases the integrated mass recovers the underlying value (shown in red), meaning that the explicit use of the constraint is not adding much new information. Figure 7(c) shows how the inferred integrated mass, for the nominal case, compares to the underlying true value for various values of r_{marker} (where the mass interior to the shock position is a constant and subtracted off). This shows that even without any explicit constraint added in the form of a Lagrangian marker, Eq. (9) is satisfied for all values of r_{marker} based only on the information stored in the lineout, so there is minimal additional information leveraged from the used of a marker layer.

C. Noise

Another factor that strongly affects the ability of an analysis procedure to constrain the density jump is random statistical noise. Specifically, an experimental radiograph is the result of a Poisson process in which photons are deposited on a streak camera detector, and this process creates a radiograph with random noise. By construction, the radiography simulation built does not contain random statistical noise, but a lineout can easily be modified to include such noise. Poisson noise is inversely proportional to the square root of the signal such that a normalized radiograph would have less noise where the value is closer to 1. This can be approximated by the following equation:

$$\text{noise} \propto \frac{\alpha}{\sqrt{\text{signal}}}, \tag{10}$$

where α is a scaling factor. The inference results where noise is included in the lineout, while also using the same marker layer constraint as Sec. VI B, are shown in Fig. 8. In this case the sampling still returns a good fit to the lineout shown in Fig. 8(c) along with a good fit to the density profile on the whole in Fig. 8(b). The posteriors shown in Fig. 8 (a) show similar general trends to the previous examples but now show a significant modal structure.

It is important to be aware of the modal structure that noise introduces into the likelihood surface, especially in the presence of point estimate inference techniques such as least squares fitting, maximum likelihood estimation, and minimum χ^2 fitting. These techniques rely on optimization routines to find regions of high probability density, often in the

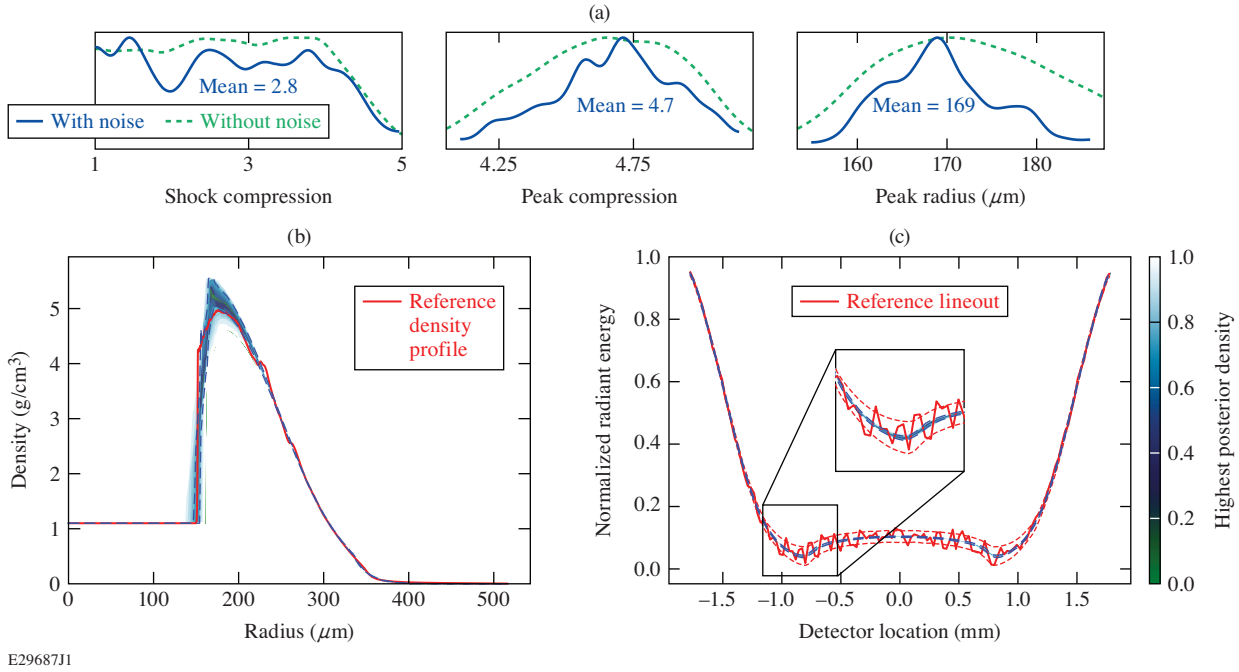

FIG. 8. (a) Posterior distributions shock compression, peak compression, and peak location, for the case with and without noise, (b) PPD's of the density profiles and (c) lineouts for the case with a Lagrangian marker and Poisson noise added to the reference lineout. The posteriors show similar general trends as in the cases without noise but now there is a distinctive modal structure present and the posteriors for peak compression and radius are both more narrow. The PPD of the density profile in (b) again shows that the density jump at the shock location is not well constrained the radial density profile on the whole is still well constrained. The comparison with the reference lineout in (c) again shows good convergence and agreement with the underlying reference. The dashed lines in (c) give the scale of σ used in the Likelihood function (e.q. 4). The modal structure in (a) is a product of the specific noise kernel used and can the locations and shapes of the modes can be expected to vary randomly.

face of approximations about the nature of the uncertainty in measurements and correlations between model parameters; and in systems with a large number of parameters, it is very likely that point estimate techniques will find a local extrema in parameter space. Additionally analysis techniques relying on these point estimates often do a local error analysis by perturbing parameters around that peak[12], a process which assumes a single dominant mode to the probability densities of the estimators. This assumption can lead to dramatic underestimates of the uncertainty on inferred parameters. As an example if a single mode of the shock compression posterior from Fig. 8 (a) is selected as the 'best-fit' as would be the case for a point estimate and a local error estimation was done the inferred uncertainty would be something akin to a normal distribution fit around that peak producing what appears to be a well constrained measurement, when in reality the posterior distribution is not well approximated by a normal distribution.

Modality is a concern for Bayesian inference techniques as well, especially depending on the sampling algorithm used. This work used a sequential Monte-Carlo sampler (also known as a particle filter), which is more well behaved in the face of multimodal posteriors than traditional Markov-chain Monte-Carlo (MCMC) techniques and the goal of the algorithm is to construct the full posterior distributions, rather than seeking an extrema, so modality is only a concern if it prevents the samplers from properly exploring the space.

D. Outside Constraint from Prior Data

The results from the previous test cases demonstrate that some additional information is needed to constrain the inferred shock compression. Figure 9 (a) shows the uniform prior distribution (green) for the shock compression, alongside the posteriors from the 3 test cases above. A defining feature of the inference from these cases is the upper-limit placed on the shock compression, which can be used in combination with outside information to constrain the posterior further.

The simplest way to introduce this outside information is by using a more informed prior distribution, for example one that introduces a lower limit on the shock compression. A naive implementation is shown in Fig. 9 (b) where the data-informed prior (orange) is simply a uniform distribution with a lower bound set by the maximum compression measurement, of 3.39[27], from previous data along the Hugoniot of CH up to 8.74 Mbar performed in planar geometry using a different methodology. Figure 9 (b) also shows the posterior for shock compression given the new prior (red), which is now significantly more peaked than the previous results (green) meaning that there is a well-defined region of high probability density.

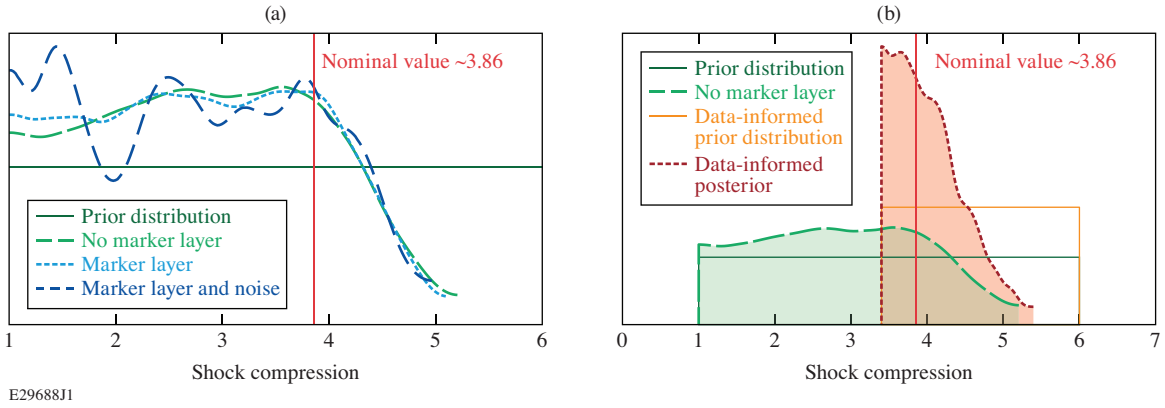

FIG. 9. (a) Posterior distributions of the shock compression (ρ_s/ρ_0) for the cases with no noise and no Lagrangian marker layer (long-dashed green), no noise with a Lagrangian marker layer (dotted light-blue), and with noise and a Lagrangian marker layer (dotted dark-blue). Also shown are the prior used for each case (solid green) and the nominal value from the *LILAC* density profile (solid red), given as 3.86. All of the distributions show the same general trend that above a compression of 4 the probability density drops sharply, due to the peak compression behind the shock being well constrained and the shock jump necessarily being smaller, effectively giving an upper bound on the shock jump. There is little constraint on the lower end of the compression where the probability density is effectively flat between 1 and 4. The case with noise shows modal structure that, if point estimates are used, can give the impression of constraint while only being a local maximum in probability density. (b) The posterior for shock compression (dashed green) for the case with a broad uniform prior (solid green) and posterior (dotted red) for the case with a narrow uniform prior (solid orange) truncated at the low end at the location of previous measurements[27]. This demonstrates how Bayesian inference allows additional information to be leveraged to constrain a quantity that is otherwise unconstrained. The combination of the prior informing a lower limit of compression and the radiograph constraining upper limits of compression results in a nicely peaked posterior probability density that captures the proper underlying value (solid red). The axes are expanded to demonstrate how the priors enforce that there is 0 probability density outside of their bounds. Note that the data-informed posterior is largely asymmetric though presents a strongly peaked result that recovers the nominal value.

VII. CONCLUSIONS

The results shown here provide insight into the information content within x-ray radiographs of spherically converging shock waves in solid-density materials. Experiments of these types have been widely used throughout the HED community and most recently have claimed to provide absolute EOS measurements based on being able to recover the compression at the location of the shock front. In the system investigated here, which can be seen as a best-case experimental scenario as discussed in Sec. V, there is insufficient information content within an x-ray radiograph lineout alone to claim measurement of the compression at the shock front. This is most clearly shown in Fig. 9(a), where the uninformed prior probability density distribution (solid green line) is plotted with the posterior probability density distributions from the different test cases presented within this work including no marker layer (light green), with a marker layer (light blue), and a reference with randomly generated noise (dark blue). It is clear that beyond placing an upper bound on the shock compression, the radiograph alone is unable to further constrain the shock compression. It also appears that when Poisson noise is introduced, different modes appear in the posterior surface that can cause analysis techniques based on point estimates and optimization schemes to converge to a local extrema, which would cause the precision of the estimate to be dramatically overestimated when local uncertainty analysis is done.

This work shows that an abundance of caution should be used when reconstructing density profiles from radiography measurements and that a priority should be placed on sampling the entirety of the likelihood surface rather than performing point estimates of parameters. Although this work investigated only one particular scale of experiment (relevant to the OMEGA laser) and performed inference on a single time slice of the radiograph, the results are unlikely to change in the face of a different scale or by leveraging the full time history of a streaked radiograph. In the case of time history, the earlier time inferences would provide a lower bound on the shock compression (until ionization effects are reached at the highest pressures) since the shock wave is strengthening as it converges, but the system is still reducible to the first time slice where the compression would be mostly unconstrained and therefore the uncertainty would propagate forward through all other times. Additionally, there would be an increased number of parameters necessary to fit the entire streak. Finally, a pathway to constraining the shock compression is presented by making use of previous data to set a lower bound on the prior of the shock compression. A converging shock experiment where the initial shock pressure is well-matched to previous experiments would allow the initial time slice to be well constrained and then subsequent times in the streaked history would be constrained by the previous time-slice, leading to a global constraint.

Although the shock compression is not strongly constrained by the radiograph alone, the density profile is well constrained by the radiograph measurement. In particular, the areal density (ρR) is very well constrained and is a quantity of particu-

lar interest within the ICF community[8]. The findings here are in excellent agreement with previous radiography measurements done on shells for the purpose of diagnosing metrics relevant to ICF modeling,[8] and this work can be seen as an extension of those efforts with additional insight into the uncertainties associated with such reconstructions. Additionally, the peak density achieved within the bulk of the material behind the shock, which has a great effect on the propagation of the outgoing shock wave,[28] is well constrained. Radiography measurements of this kind contain a great deal of information that can be used in combination with other measurements to develop a full picture of implosion experiments, including how materials respond to strong converging shock waves.

This work can be used as a foundation to develop further investigations about the information contained in measurements of this type. Experimentally additional information can be introduced using phase contrast imaging (also known as refraction enhanced radiography)[10,11,29] to better constrain the density at the shock jump. In these systems there is an additional feature in the radiograph that is sensitive to the derivative of the density profile in space meaning that it is very sensitive to the jump at the shock front where the gradient is very large. This work can aid experimental design by giving a platform to test which aspects of the design help constrain particular quantities of interest, for example in this case by showing that the Lagrangian marker layer does not introduce much new information so is likely not worth the effort of target fabrication, and can be used as a foundation to leverage heterogeneous information to maximize what we can learn about the high-energy-density matter achieved in these complex implosion experiments.

VIII. ACKNOWLEDGMENTS

The authors extend their gratitude to David Bishel and Ethan Smith for their aid in the development in the ray-trace software used in this work.

This material is based upon work supported by the Department of Energy National Nuclear Security Administration under Award Number DE-NA0003856, the U.S. Department of Energy, Office of Science, Office of Fusion Energy Sciences under Award No. DE-SC001926, the University of Rochester, and the New York State Energy Research and Development Authority.

[1] W. Roentgen, "On a new kind of rays," Nature **53**, 274–276 (1896).

[2] S. C. Mayo, A. W. Stevenson, and S. W. Wilkins, "In-line phase-contrast x-ray imaging and tomography for materials science," Materials **5**, 937–965 (2012).

[3] C. A. Roobottom, G. Mitchell, and G. Morgan-Hughes, "Radiation-reduction strategies in cardiac computed tomographic angiography," Clin. Radiol. **65**, 859–867 (2010), number of radiographic investigations performed.

[4] A. F. T. Leong, E. Asare, R. Rex, X. H. Xiao, K. T. Ramesh, and T. C. Hufnagel, "Determination of size distributions of non-spherical pores or particles from single x-ray phase contrast images," Optics Express **27**, 17322 (2019).

[5] M. V. Geet, R. Swennen, and M. Wevers, "Towards 3-d petrography: Application of microfocus computer tomography in geological science," Computers and Geosciences **27**, 1091–1099 (2001).

[6] B. A. Hammel, D. Griswold, O. L. Landen, T. S. Perry, B. A. Remington, P. L. Miller, T. A. Peyser, and J. D. Kilkenny, "X-ray radiographic measurements of radiation-driven shock and interface motion in solid density material," Physics of Fluids B **5**, 2259–2264 (1993), <br/>.

[7] F. J. Marshall, P. W. McKenty, J. A. Delettrez, R. Epstein, J. P. Knauer, V. A. Smalyuk, J. A. Frenje, C. K. Li, R. D. Petrasso, F. H. Séguin, and R. C. Mancini, "Plasma-density determination from x-ray radiography of laser-driven spherical implosions," Physical Review Letters **102** (2009), 10.1103/PhysRevLett.102.185004.

[8] D. G. Hicks, B. K. Spears, D. G. Braun, R. E. Olson, C. M. Sorce, P. M. Celliers, G. W. Collins, and O. L. Landen, "Convergent ablator performance measurements," Physics of Plasmas **17** (2010), 10.1063/1.3486536.

[9] J. A. Koch, O. L. Landen, B. J. Kozioziemski, N. Izumi, E. L. Dewald, J. D. Salmonson, and B. A. Hammel, "Refraction-enhanced x-ray radiography for inertial confinement fusion and laser-produced plasma applications," Journal of Applied Physics **105** (2009), 10.1063/1.3133092.

[10] E. L. Dewald, O. L. Landen, L. Masse, D. Ho, Y. Ping, D. Thorn, N. Izumi, L. B. Hopkins, J. Kroll, A. Nikroo, and J. A. Koch, "X-ray streaked refraction enhanced radiography for inferring inflight density gradients in icf capsule implosions," Review of Scientific Instruments **89** (2018), 10.1063/1.5039346.

[11] Y. Ping, L. Landen, G. Hicks, A. Koch, R. Wallace, C. Sorce, A. Hammel, and W. Collins, "Refraction-enhanced x-ray radiography for density profile measurements at CH/Be interface," Journal of Instrumentation **6** (2011), 10.1088/1748-0221/6/09/P09004.

[12] D. C. Swift, A. L. Kritcher, J. A. Hawreliak, A. Lazicki, A. Macphee, B. Bachmann, T. Döppner, J. Nilsen, G. W. Collins, S. Glenzer, S. D. Rothman, D. Kraus, and R. W. Falcone, "Absolute hugoniot measurements from a spherically convergent shock using x-ray radiography," Review of Scientific Instruments **89** (2018), 10.1063/1.5032142.

[13] T. Döppner, D. C. Swift, A. L. Kritcher, B. Bachmann, G. W. Collins, D. A. Chapman, J. Hawreliak, D. Kraus, J. Nilsen, S. Rothman, L. X. Benedict, E. Dewald, D. E. Fratanduono, J. A. Gaffney, S. H. Glenzer, S. Hamel, O. L. Landen, H. J. Lee, S. Lepape, T. Ma, M. J. Macdonald, A. G. Macphee, D. Milathianaki, M. Millot, P. Neumayer, P. A. Sterne, R. Tommasini, and R. W. Falcone, "Absolute equation-of-state measurement for polystyrene from 25 to 60 mbar using a spherically converging shock wave," Physical Review Letters **121** (2018), 10.1103/PhysRevLett.121.025001.

[14] A. L. Kritcher, D. C. Swift, T. Döppner, B. Bachmann, L. X. Benedict, G. W. Collins, J. L. DuBois, F. Elsner, G. Fontaine, J. A. Gaffney, S. Hamel, A. Lazicki, W. R. Johnson, N. Kostinski, D. Kraus, M. J. MacDonald, B. Maddox, M. E. Martin, P. Neumayer, A. Nikroo, J. Nilsen, B. A. Remington, D. Saumon, P. A. Sterne, W. Sweet, A. A. Correa, H. D. Whitley, R. W. Falcone, and S. H. Glenzer, "A measurement of the equation of state of carbon envelopes of white dwarfs," Nature **584**, 51–54 (2020).

[15] Y. P. Raizer and Y. B. Zel'dovich, *Physics of shock waves and high-temperature hydrodynamic phenomena* (Academic Press, New York, NY, 1967) trans. from the Russian.

[16] T. R. Boehly, D. L. Brown, R. S. Craxton, R. L. Keck, J. P. Knauer, J. H. Kelly, T. J. Kessler, S. A. Kumpan, S. J. Loucks, S. A. Letzring, F. J. Marshall, R. L. McCrory, S. F. Morse, W. Seka, J. M. Soures, and C. P. Verdon, "Initial performance results of the OMEGA laser system," Optics Communications **133**, 495–506 (1997).

[17] J. E. Field, J. R. Rygg, M. A. Barrios, L. R. Benedetti, T. Döppner, N. Izumi, O. Jones, S. F. Khan, T. Ma, S. R. Nagel, A. Pak, R. Tommasini, D. K. Bradley, and R. P. Town, "Reconstruction of 2D x-ray radiographs at the National Ignition Facility using pinhole tomography (invited)," Review of Scientific Instruments **85**, 1–6 (2014).

[18] J. R. Rygg, O. S. Jones, J. E. Field, M. A. Barrios, L. R. Benedetti, G. W. Collins, D. C. Eder, M. J. Edwards, J. L. Kline, J. J. Kroll, O. L. Landen, T. Ma, A. Pak, J. L. Peterson, K. Raman, R. P. Town, and D. K. Bradley, "2d x-ray radiography of imploding capsules at the national ignition facility," Physical Review Letters **112** (2014), 10.1103/PhysRevLett.112.195001.

[19] D. Mihalas, *Stellar Atmospheres* (W. H. Freeman, San Francisco, CA, 1978).

[20] L. for Laser Energetics, "The ross streak camera," (2006).

[21] J. D. Kilkenny, "High speed proximity focused x-ray cameras," Laser and Particle Beams **9**, 49–69 (1991).

[22] P. Knapp, "Primer on bayesian inference and applications to data analysis," (2020).

[23] J. Ruby, J. Rygg, D. Chin, J. Gaffney, P. Adrian, D. Bishel, C. Forrest, V. Glebov, N. Kabadi, P. Nilson, Y. Ping, C. Stoeckl, and G. Collins, "Constraining physical models at gigabar pressures," Physical Review E **102**, 53210 (2020).

[24] J. A. Gaffney, D. Clark, V. Sonnad, and S. B. Libby, "Bayesian Analysis of Inertial Confinement Fusion Experiments at the National Ignition Facility," arXiv preprint arXiv:1207.0532 (2012), arXiv:arXiv:1207.0532v1.

[25] B. Bennett, J. Johnson, G. Kerley, and G. Rood, "Sesame: the Los Alamos National Laboratory equation of state database," Los Alamos National Laboratory, Los Alamos, NM, LA- … , 43 (1992).

[26] J. Colgan, D. P. Kilcrease, N. H. Magee, M. E. Sherrill, J. Abdallah Jr., P. Hakel, C. J. Fontes, J. A. Guzik, and K. A. Mussack, "a New Generation of Los Alamos Opacity Tables," The Astrophysical Journal **817**, 116 (2016), arXiv:1601.01005.

[27] M. A. Barrios, D. G. Hicks, T. R. Boehly, D. E. Fratanduono, J. H. Eggert, P. M. Celliers, G. W. Collins, and D. D. Meyerhofer, "High-precision measurements of the equation of state of hydrocarbons at 1-10 Mbar using laser-driven shock waves," Physics of Plasmas **17** (2010), 10.1063/1.3358144.

[28] J. Ruby, J. Rygg, J. Gaffney, B. Bachmann, and G. Collins, "A boundary condition for Guderley's converging shock problem," Physics of Fluids **31** (2019), 10.1063/1.5130769.

[29] L. Antonelli, F. Barbato, D. Mancelli, J. Trela, G. Zeraouli, G. Boutoux, P. Neumayer, S. Atzeni, A. Schiavi, L. Volpe, V. Bagnoud, C. Brabetz, B. Zielbauer, P. Bradford, N. Woolsey, B. Borm, and D. Batani, "X-ray phase-contrast imaging for laser-induced shock waves," EPL **125** (2019), 10.1209/0295-5075/125/35002.

[30] Y. Ping, V. A. Smalyuk, P. Amendt, R. Tommasini, J. E. Field, S. Khan, D. Bennett, E. Dewald, F. Graziani, S. Johnson, O. L. Landen, A. G. MacPhee, A. Nikroo, J. Pino, S. Prisbrey, J. Ralph, R. Seugling, D. Strozzi, R. E. Tipton, Y. M. Wang, E. Loomis, E. Merritt, and D. Montgomery, "Enhanced energy coupling for indirectly driven inertial confinement fusion," Nature Physics **15**, 138–141 (2019).